Understanding nanoscale oxide build up on EUROFER97

Patricia Jovičević-Klug [a,b,*,1] ⓘ, Cristiano Kasdorf Giesbrecht [a,1], J. Manoj Prabhakar [a,1],
Tim M. Schwarz [a] ⓘ, Carsten Bonnekoh [c] ⓘ, Michael Rieth [c] ⓘ, Michael Rohwerder [a] ⓘ

[a] *Max Planck Institute for Sustainable Materials (Max-Planck-Institut für Eisenforschung GmbH), Max-Planck-Straße 1, Düsseldorf 40237, Germany*
[b] *Alexander von Humboldt Postdoc Research Fellow, Alexander von Humboldt Foundation, Jean-Paul-Straße 12, Bonn 53173, Germany*
[c] *Institute for Applied Materials, Karlsruhe Institute of Technology, Hermann-von-Helmholtz-Platz 1, Eggenstein-Leopoldshafen 76344, Germany*

ABSTRACT

Delivering nuclear fusion requires the development of new materials. EUROFER97 is a prime candidate for first wall and structural applications, yet it needs improved corrosion resistance. Here we show how cryogenic processing (CP) changes the evolution of the native oxide layer before and after exposure to aqueous NaCl, with Fe and N now controlling the oxide formation, instead of Cr and Ce in the control sample. The N introduced into the matrix by the CP also results in increased corrosion resistance, as indicated by potentiodynamic corrosion resistance measurements.

1. Introduction

The advanced reduced activation ferritic-martensitic (RAFM) 9 % Cr steels, such as EUROFER97, are planned to be used as part of the first wall in fusion reactors[1]. The reason for this is its superior properties, such as thermo-physical and mechanical properties[2], good compatibility with other materials and low sensitivity to radiation-induced swelling[2,3]. The reason lies in a unique microstructure that comprises a matrix and tailored precipitation. The main precipitates are $M_{23}C_6$ carbides, nitrides, carbonitrides and also smaller amounts of other types of carbides[4–6]. Furthermore, safety and reliable operation of the fusion system are highly dependent on the performance of the materials in the extreme conditions, i.e. high temperature, high pressure and highly corrosive environment. In relation to corrosion and EUROFER97, some studies have been carried out which have shown that high Cr values within the steel play an important role in the corrosion resistance of EUROFER97[7]. According to corrosion studies by Mukai et al. [8] and Duerrschnabel et al. [9] of EUROFER97, showed that two layers are formed in Li enriched environment. The first, i.e. the outermost layer is enriched with Fe and the inner layer is enriched with Cr-oxides. The study by Ningshen et al. [7] showed with X-ray photoelectron spectroscopy (XPS) that the Cr enriched oxide layer, when exposed in NaCl, is mainly enriched with Cr_2O_3 oxide type.

Furthermore, Hernández et al. [10] showed that the corrosion zone of EUROFER97 also contains hematite (α-Fe_2O_3) and magnetite (Fe_3O_4) Fe-oxides and the presence of more complex and mixed oxides. It is also noted that the layer of the Fe-oxides becomes denser and compact over time compared to the Cr oxide layer[10]. However, the higher Cr content in many conventional steels can also have a detrimental effect on the steel, causing thermal ageing embrittlement[11,12]. Despite the high Cr content, EUROFER97 does not form a sigma phase, which can have a negative effect on the final properties[11,12]. Furthermore, a study by Terada et al. [13] also shows that the good corrosion resistance of EUROFER97 in NaCl is correlated with the lower number of carbides compared to the other types of EUROFER97, which is related to the location of carbide precipitation at the grain boundaries, which supposedly leads to the reduced corrosion resistance.

In the past, chloride salts were not much considered as a melting medium, but some studies[14] have shown that they have a lower melting point, which is more of an advantage than a disadvantage. The typical derivatives of chloride salts are ClLiBe, ClLiNa, ClLiK and ClLiPb, where K and Na are abundant and inexpensive[14]. A large variety of Fe oxides and passivation layers has been studied to some extent for EUROFER97, but one of the most powerful tools for analysing metal surfaces, Fourier Transform Infrared Spectroscopy[15] (FT-IR), has not, to our knowledge, been used for this purpose. FT-IR can show complex

---

* Corresponding author at: Max Planck Institute for Sustainable Materials (Max-Planck-Institut für Eisenforschung GmbH), Max-Planck-Straße 1, Düsseldorf 40237, Germany.

E-mail address: p.jovicevic-klug@mpie.de (P. Jovičević-Klug).

[1] authors contributed to the manuscript equally

molecular peaks in addition to typical oxides, which can be advantageous in understanding the complex passivation dynamics of EUROFER97. Although corrosion behaviour of EUROFER97 steel has been studied before[13,16], cryogenic processing (CP) and its influence on the passivation layer and the corrosion resistance and Fe oxide dynamics hasn't been well researched. Furthermore, the possible manipulation of the passivation layer by CP in relation to EUROFER97 literature does not exist yet (to our knowledge). There have been some studies on CP and corrosion resistance, which have shown for tool steels that CP has an influence on the passive layer and layering of oxides, such as green rust and magnetite, which has been shown to be beneficial for corrosion or even tribocorrosion resistance for selected tool steels[17–19]. It is important to note that there are studies where the material is tested at cryogenic temperatures in the final stage, rather than being treated at cryogenic temperature to tailor its microstructure.

This study investigates the corrosion behaviour of EUROFER97 in 30 wt% NaCl containing environment. Specifically, the study and experiments were designed to examine the passive layer formation during a short-term corrosion study of EUROFER97 at room temperature. The oxide layer was examined using scanning electron microscopy (SEM), energy dispersive X-ray spectroscopy (EDS), XPS, angle resolved XPS (AR-XPS) and profile XPS in correlation with Raman spectroscopy, FT-IR and potentiodynamic polarization measurements. The microstructure was also examined using atom probe tomography (APT) to provide a detailed correlation. The study shows the different development of the native oxide layer before and after the application of NaCl in the control and test samples. In the CP-treated sample, the important role of oxide formation is shifted to Fe and N, compared to the control sample where Cr and Ce oxides also play an important role.

2. Methods

2.1. Material, processing and surface analysis

EUROFER97 (in the following text abbreviates as EF) is a RAFM Cr-rich iron alloy (actual measured chemical composition in wt%: 0.11 C, 0.4 Mn, 9 Cr, 0.12 Ta, 1.1 W, 0.03 N, 0.15 V, base Fe, other elements <0.012) and was provided by the Karlsruhe Institute of Technology (KIT), Germany [20]. EUROFER97 material was melted in 16-ton vacuum induction furnaces, then remelted in a vacuum arc furnace and forged into billets and then rolled. Heats of plate material were then prepared and samples taken for chemical and other analysis. The EUROFER97 samples were then divided into two sub-groups for the purpose of testing and observing oxide formation based on different heat treatment processes. Heat treatment was carried out in a controlled environment in a vacuum furnace with Ar, where the quenching rate can be controlled and adjusted. Control-EF and test-EF, where the austenitisation temperature was Ta= 1273 K for 30 min and quenching rate 6 K/s (1073–823 K in ~ 40 s). Afterwards control-EF was subjected immediately subjected to 1 cycle tempering at 823 K for 120 min while the other sub-group test-EF was firstly subjected to CP for 1 day at 77 K. After CP, the test-EF group underwent 1 cycle of tempering under the same conditions as control-EF. At the Max Planck Institute for Sustainable Materials (MPI SusMat), Germany, the samples were heat treated. The heat treatment of both sub-groups was carried out in an Ar atmosphere. This was done in order to eliminate the influence of the N_2 gas on the microstructure during the quenching and tempering process. The specimens were metallographically prepared for further analysis following Jovičević-Klug et al. [19] for preparing cryogenically treated ferrous alloys for microstructural analysis and surface analysis. A scanning electron microscope (SEM) Zeiss Merlin I and Merlin II was used for the microstructural analysis of the EUROFER97 alloy at the MPI SusMat, Germany. In order to test the corrosion species, two experiments were done, one without and another one in 30 wt% NaCl aqueous solution for 1 day in environment with ambient conditions (21 °C and 50 % relative humidity). The 30 wt% NaCl solution was selected and was found to be

very effective in initiating corrosion of the sample within the given time and may be comparable to more aggressive salts.

2.2. Atom probe tomography

APT specimens were prepared according to the standard specimen preparation protocol described by Thompson et al. [21] using a Ga FIB (Helios 5 CX). A Cameca LEAP 5000 XR series atom probe was used for the APT experiments. The APT measurement was performed in laser pulse mode with 20–40 pJ laser energy with repetition rate of 100 kHz at 40 K base sample temperature with an average detection rate of 1.0 ion per 100 pulses. Cameca's Integrated Visualisation and Analysis Software (IVAS) in AP Suite 6.3 was used for data reconstruction.

2.3. Fourier transform infrared spectroscopy

Fourier Transform Infrared Spectroscopy (FT-IR) measurements were performed using a spectrometer model VERTEX 70 v, Bruker Optik GmbH, Ettlingen, Germany. The IR beam was guided out from the spectrometer to an external analysis chamber equipped with a sample manipulator (adjustable in vertical and horizontal axes and in angle) and to an external detector chamber, which can be flushed with different atmosphere and was built in house.

This detector was an LN-MCT (liquid N_2 cooled HgCdTe) detector. The analysis chamber containing the sample was flushed with dry Ar atmosphere at a rate of 40 ln/h. The sample was fixed on a sample holder with Cu tape, introduced into the system and transferred to the analysis chamber, where it was adjusted until the detector showed a good signal intensity. The complete system for the IR is presented In Fig. 1. For this study, the spectrometer was configured with 4 cm^{-1} resolution and 2 mm aperture, using a KBr beam splitter and a mid-infrared (MIR) light source. The spectra acquisition was performed one hour after the LN-MCT detector has been cooled down with liquid nitrogen; these data were acquired by 1024 scans repeated ten times. The same procedure was performed for the background analysis on a freshly polished sample before the corrosion process and for sample after corrosion.

2.4. Raman shift spectroscopy

Raman shift spectroscopy was performed using a LabRAM confocal Raman microscopy system from Horiba Jobin Yvon, France. The system was equipped with a 50 × objective. It had a 600 L mm^{-1} grating and a charge coupled device (CCD) detector. A HeNe laser was used for the measurements. The wavelength of the laser was λ = 532 nm. Focused on a sample area of 10 μm^2, the spot laser power was approximately 6 mW. Data were collected with an accumulation time of 3 × 600 s and a spectral resolution of approximately 1 cm^{-1}. The Raman spectroscopic database library RRUFF was used for the identification of oxides.

2.5. X-ray photoelectron spectroscopy and scanning auger microscopy

X-ray photoelectron spectroscopy (XPS) was performed in a Physical Electronics PHI Quantera II spectrometer equipped with an Al Kα source at 1486.6 eV. A pass energy of 26 eV was used to record the O (O 1 s), Na (Na 2 s), N (N 1 s) core level spectra. The Fe (Fe 2p$_{3/2}$), Cr (Cr 2p$_{3/2}$), Ta (Ta 4 f$_{7/2}$), Ce (Ce 3d$_{5/2}$) and Cl (Cl 2p$_{3/2}$) core spectra were obtained with a pass energy of 55 eV. A pass energy of 112 eV was used to acquire the survey scan spectra. All measurements were taken at an incident angle of 45°. XPS depth profiling was performed by etching the sample with an Ar ion beam of 2 kV energy on an area of 2 mm × 2 mm for different time intervals (0–120 s). Angle resolved XPS (AR-XPS) was done in angles 0°, 15°, 30°, 45°, 60°, 75° and 90°. The smaller angles (e.g.15°) were chosen to obtain more information from the oxide layer, i.e. the surface layer, while greater angles (e.g. 90°) were chosen to obtain spectral information relating to the bulk of the samples. The peaks of the XPS spectra were fitted with the CasaXPS software version 2.3.22,
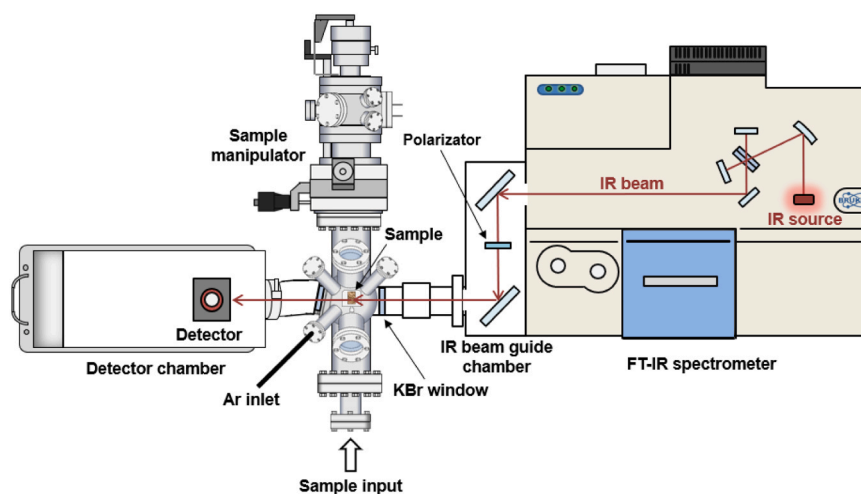
Fig. 1. Representation of the FT-IR setup with its main components and the sample analysis and external detector chambers employed in the present study.

applying the Shirley-type background to all spectra. A Gaussian (70 %)—Lorentzian (30 %) peak shape was used for the symmetrical components. A Lorentzian Asymmetric, LA(1,3,4,5), peak shape was used for the metallic Fe component to account for the asymmetric metallic peak. In addition, to distinguish small peaks (e.g. N1s) and shifts, detailed analysis was performed according to Major et al. [22], Tougaard [23] and Pinder et al. [24].

Scanning Auger microscopy (SAM) was performed utilizing a JEOL JAMP 9500-F scanning Auger microprobe to generate high-resolution elemental maps of Cr, Ta, Fe, Ce, O and N. Each elemental map was produced by scanning for a corresponding Auger peak across the area at a resolution of 256 × 256 (256 lines with 256 points per line). The final elemental distribution maps are created by superimposing the individual elemental maps.

2.6. Potentiodynamic polarization

Potentiodynamic polarization measurements were carried out using a Vertex One potentiostat from Ivium technologies on metallurgically prepared samples according to Jovičević-Klug et al. [19]. The sample was placed in an electrochemical cell, where an area of 0.2829 cm² was exposed to the electrolyte using an O-ring of diameter 6 mm. The sample in contact with 30 wt% NaCl aqueous aerated solution at environment with ambient conditions (21 °C and 50 % relative humidity) was stabilized for 30 mins to obtain the open circuit potential and the potentiodynamic polarization was carried out from −1.04 V vs Ag/AgCl to −0.35 V vs Ag/AgCl at a scan rate of 1 mV/s. The solution volume used was 25 mL. Tafel extrapolation was carried out to obtain the corrosion current density and corrosion potential of the samples from the plots.

3. Results and discussion

3.1. Exploring the relationship between microstructure and native oxide

Detailed microstructural and advanced microstructural analyses have already been performed in our previous papers Jovičević-Klug et al. [4],[25], using various techniques such as SEM, electron backscatter diffraction (EBSD), transmission electron microscopy (TEM), X-ray diffraction (XRD) and APT However, in order to understand the evolution and influence of chemistry and microstructure on the development of the native oxide and later passive film, the most important aspects are presented here (Fig. 2) with additional and detailed studies of Ce-oxide(s) using SAM and APT. Both heat treatment groups have martensite as the main phase and about 1 % retained austenite. In both cases, the matrix is enriched with Fe and Cr as the main alloying

elements, all other alloying elements being less than 1 at% (Table 1). The EDS results also indicate that Cr is depleted in test-EF samples, and enriched with Fe compare to the control-EF sample, which is correlated to the cryogenic processing.

In the matrix composition of the test-EF sample (based on our detailed microstructural study in previous two articles), the depletion of Cr can be observed, which is correlated with the increased precipitation of carbides (mainly $M_{23}C_6$) due to the cryogenic processing (Fig. 2**b-c**). The main types are M_6C (Fe, Cr and W), MCN (Ta and/or V), M_7C_3 (Cr and Fe), M_3C_2 (Cr and Fe) and $M_{23}C_6$ (see Fig. 2**c**). The carbides are mainly precipitated on prior austenitic grains (PAG), but nanoscopic $M_{23}C_6$ is also present in the martensitic laths[4]. The ratio of the main alloying elements is important, as they will form the native oxides and later the oxides induced by the selected saline medium (in this case 30 wt% NaCl).

Individual Ce-oxides enriched in different ratio of rare earth elements (REEs) can also be observed in both samples, which were added for easier manufacturability of the steel and refinement of microstructure (Fig. 2**d-f**), in order to remove O and S from the matrix[26,27]. Therefore, there is a higher content of REEs in the Ce-oxides observed in this alloy (Fig. 2**f** and Fig. 3). This means that the oxides act as an isolated system, as the presence of REEs can only be detected within the oxides and not in the matrix or precipitates. However, the presence of Ce-oxides can be beneficial as they can act as an effective cathode, ultimately improving the corrosion resistance of the alloy[27–33]. SAM results provided the first indications that the Ce-oxides are also enriched with elements such as N, Ta and Cr. In-detail study with cross-section of one of the Ce-oxide showed/confirmed that the Ce-oxides were formed above the carbides present within the matrix, which has been also proven by APT (Fig. 2**g**). In Fig. 3 can be seen that Ce-oxide was formed on the M_6C carbide, which is enriched with Cr, Fe and W.

APT measurement of the Ce-oxide particle (Fig. 3) showed an outer (core) and inner shell structure with different partitioning of different REEs. The core structure consists of an REO oxide with a 1:1 stoichiometry, but it is known that oxygen is underrepresented in the APT due to the formation of neutral oxygen during the field evaporation process and therefore cannot be detected[34,35]. However, the main core elements are Ce and Nd in equal concentrations of about 19 at%, 8 at% Pr and approx. 3 at% La. While the main elements in the shell structure are Ta and Ce with 17.65 at% and 26.6 at% respectively, it is interesting to note that there is also an enrichment of nitrogen and carbon in the shell structure (Fig. 3). In addition, La enriched precipitates/particles were observed in the shell structure. An exact compositional analysis of the shell structure is very challenging as many of the signals in the mass spectrum could not be unambiguously assigned (see Supplementary
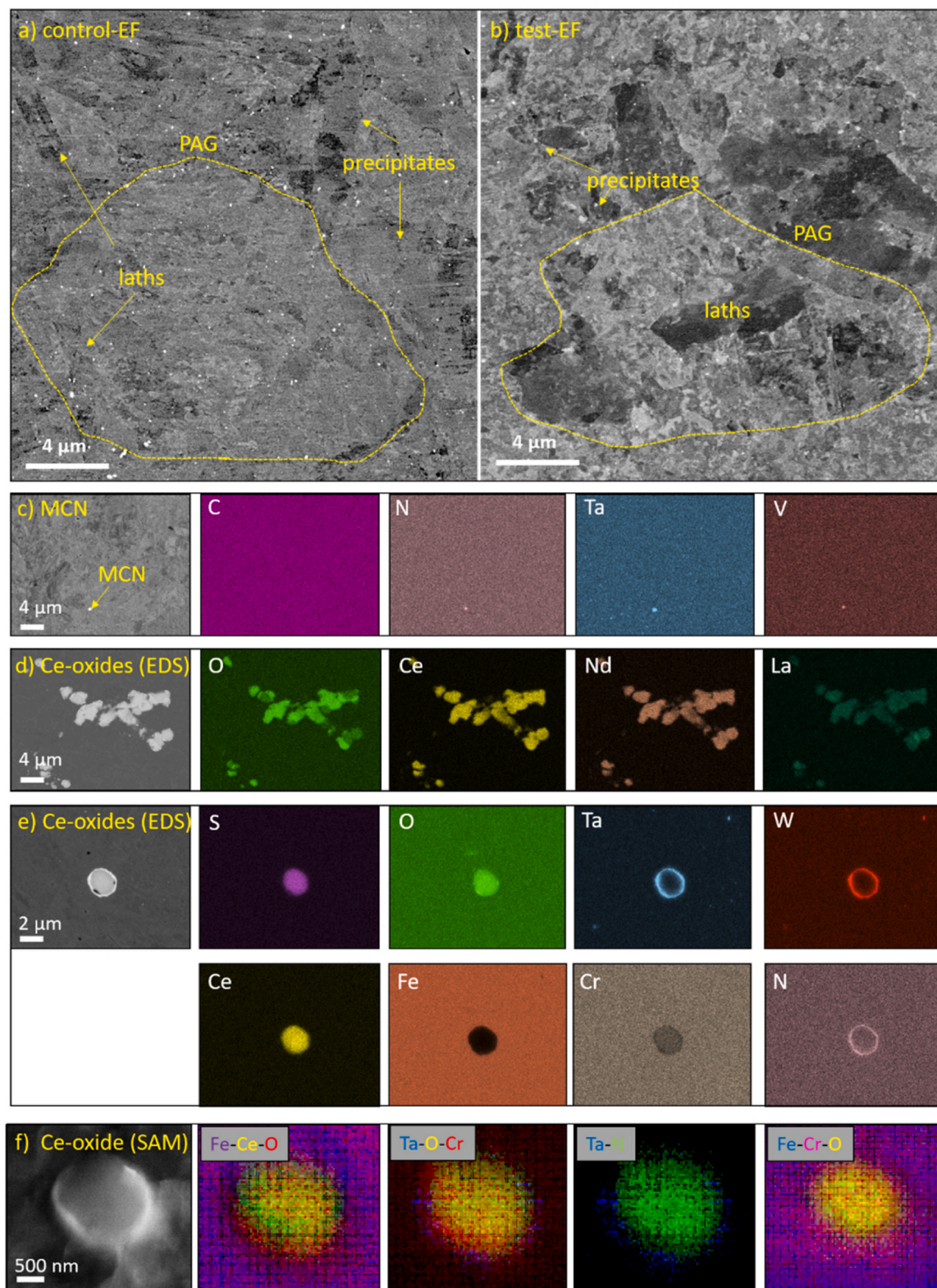
Fig. 2. The micrographs of the two samples a) control sample (control-EF) and b) tested sample (test-EF). In both micrographs the prior austenitic grains (PAG) are marked, precipitates which are mainly located at the grain boundaries as marked and martensitic lamellae. c) EDS mapping showing the MCN precipitates enriched with Ta and V. d) Ce oxides can be present in the chains or individually (e). d-e) Ce-oxides mapping obtained by EDS. f) Ce-oxide mapping done by SAM for selected elements. g) APT results show that Ce-oxides built up location is above carbide, which is mainly build-up by Fe, C, Cr and W.

Table 1
The EDS results show the chemical composition in at% for both groups' matrix, where the deficit of Cr in matrix can be clearly observed for the test-EF sample, which is attributed to the increased precipitation of carbides, compared to the control-EF sample, where additional precipitation was not observed.

Samples' matrix composition (at %)	Fe	Cr	Other alloying elements
control-EF	79.1 ± 1.2	20.5 ± 2.5	< 1
test-EF	84.5 ± 1.1	14.7 ± 2.5	< 1

Material 1) and require further analysis with different techniques. These REEs in general were only detected in the Ce-oxide core-shell structure and are not present in the matrix. Regions containing Ce oxides can act as a source of Ce, which can be activated in corrosive media to form a passivation layer [30,32,33]. The composition of the alloy based on the APT analysis shows for the matrix 90.11 at% Fe, 8.44 at% Cr, 0.28 at% W, 0.10 at% V and the remaining amount consists of impurities of Si, Al, Mn, Co and Ni, no signals of REEs could be observed in the mass spectrum (see Supplementary Material 1). In the 3D reconstruction of the APT measurement showed that the Ce-oxides were formed above the carbides present within the matrix (Fig. 3). This indicates and confirms that REEs have a high affinity to oxygen and can form complex oxides and also the interface can be the so-called rich carbo-oxide interface, which in some cases can also act as heterogeneous cores of RA under certain conditions, as suggested by Hufenbach et al. [36], which can have later an influence on the EUROFER97 final properties. The composition of the observed carbide suggested a M_6C carbide with the following composition 55 at% Cr and 25 at% and 15 at% C and about 1.5 at% W and some tracers of Mn and V. Secondly, oxide particles were observed in the Fe-Cr matrix following the composition of 64 at% O, 19–20 at% V and 10 at% N.

3.2. Analysis of the native oxide layer at ambient conditions

Fig. 4a-b shows, the curve-fitted $O1s$, $Cr2p_{3/2}$, $N1s$ and $Fe2p_{3/2}$ of in-depth etched spectra of conventionally (control-EF) and cryogenically processed (test-EF) samples (see Methods and Supplementary Material

2a-b for survey(s)). The XPS analysis was performed to identify potential detrimental species and passivation layer forming species, for which two experiments were performed.

The native oxide XPS profile (Supplementary Material 3a-b) shows the thickness of the native oxide layers (based on $O1s$ and $Fe2p$ profiles selected as indicators of native oxide) for both samples, control-EF and test-EF (with CP), taking into account the sputtering rate of 1 nm min-1. The thickness of the control EF was estimated to be 0.50 nm and that of the test-EF (with CP) to be approximately 0.52 nm.

The spectra for $O1s$ for both samples show (Fig. 4a-b) the presence of metal oxides, hydroxides/carbonates and nitrates, where low intensive nitrates peak was detected only after 120 s etching of the sample (0–120 s with 30 s interval). For $Cr2p_{3/2}$ spectra for both samples (Fig. 4a-b) and both etching times showed presence of metal, Cr (III) oxide and Cr (IV) oxide. An interesting observation was made for the $N1s$ spectra, where for the test-EF (Fig. 4a-b), an additional peak was present for both etching times, which are oxides, compared to the control-EF, where only metal nitrides are present. Furthermore, for $Fe2p_{3/2}$ for both samples (control-EF and test-EF) presence of metal peak, Fe (II) oxide and Fe (III) oxide was observed (Fig. 4a-b). Etching profiles of $O1s$ of both samples (Fig. 4c-d) show higher presence of hydroxides/carbonates in the upper layers of the profile and higher presence of metal peak at the end of etching. The interesting observation was that in the control-EF sample the higher presence of the nitrate peak is in the uppermost surface layer, whereas in the test-EF sample an increased presence of nitrates is detected towards the bulk (Fig. 4c-d). The depth profile of $Cr2p_{3/2}$ peak showed a similar trend for both samples with higher presence of Cr (III) and Cr (IV) oxides in the surface layer and metal peak towards bulk of the material (Fig. 4c1&d1). To check the oxidation dynamics and presence in the native oxide layer, Ta and Ce were also monitored. Ta as one of the main alloying elements in the alloy and Ce as the element that forms Ce-oxides and is added for higher corrosion resistance. Ta in-depth spectra ($Ta4f_{7/2}$) showed for both sample (Fig. 4c2&d2) similar trend with higher presence of Ta oxides and Ta nitrides in upper most layers and higher metallic peak towards bulk of the material. However, main difference was that the Ta oxide peak was in the control-EF sample still present after 120 s of etching, whereas in test-EF this peak is gone already after 60 s (Fig. 4c3&d3). For $Fe3p_{3/2}$ peak for both samples the presence of metal, Fe (II) and Fe (III)
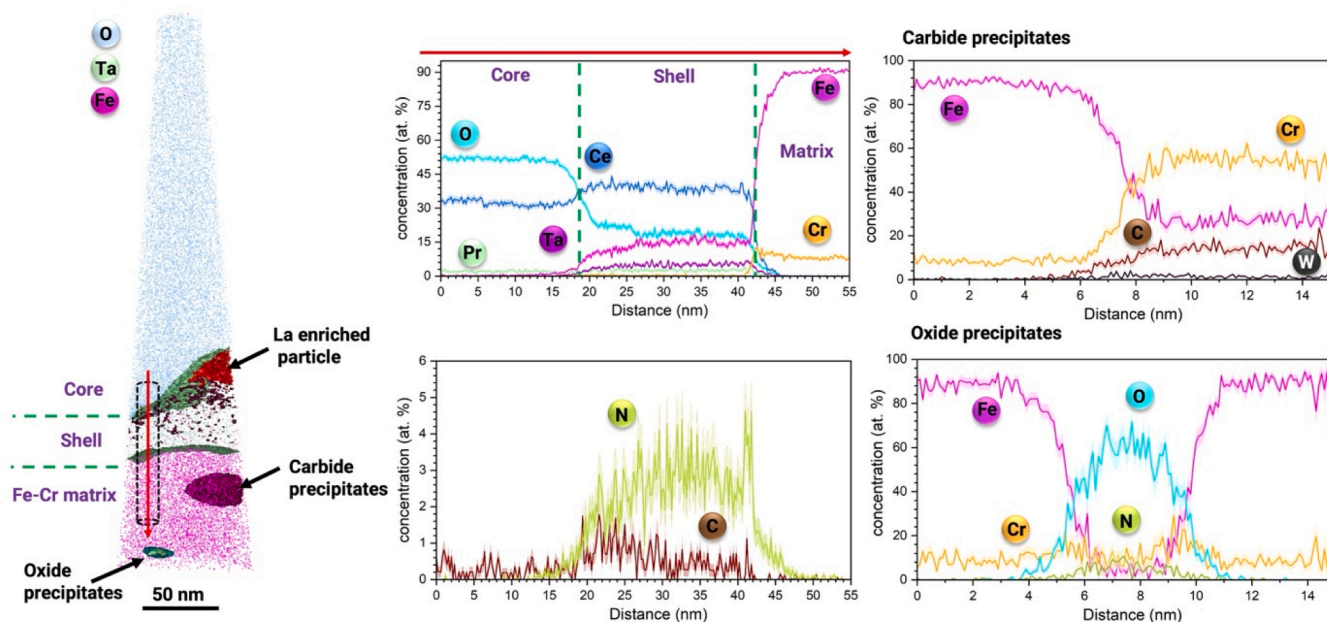

Fig. 3. 3D reconstruction of the core-shell structure of the Ce-oxide particle in the EUROFER97 alloy, where Ta is enriched in the shell structure, as well as La-rich particles. In the Fe-Cr matrix different oxide particles and carbide particles could be observed.
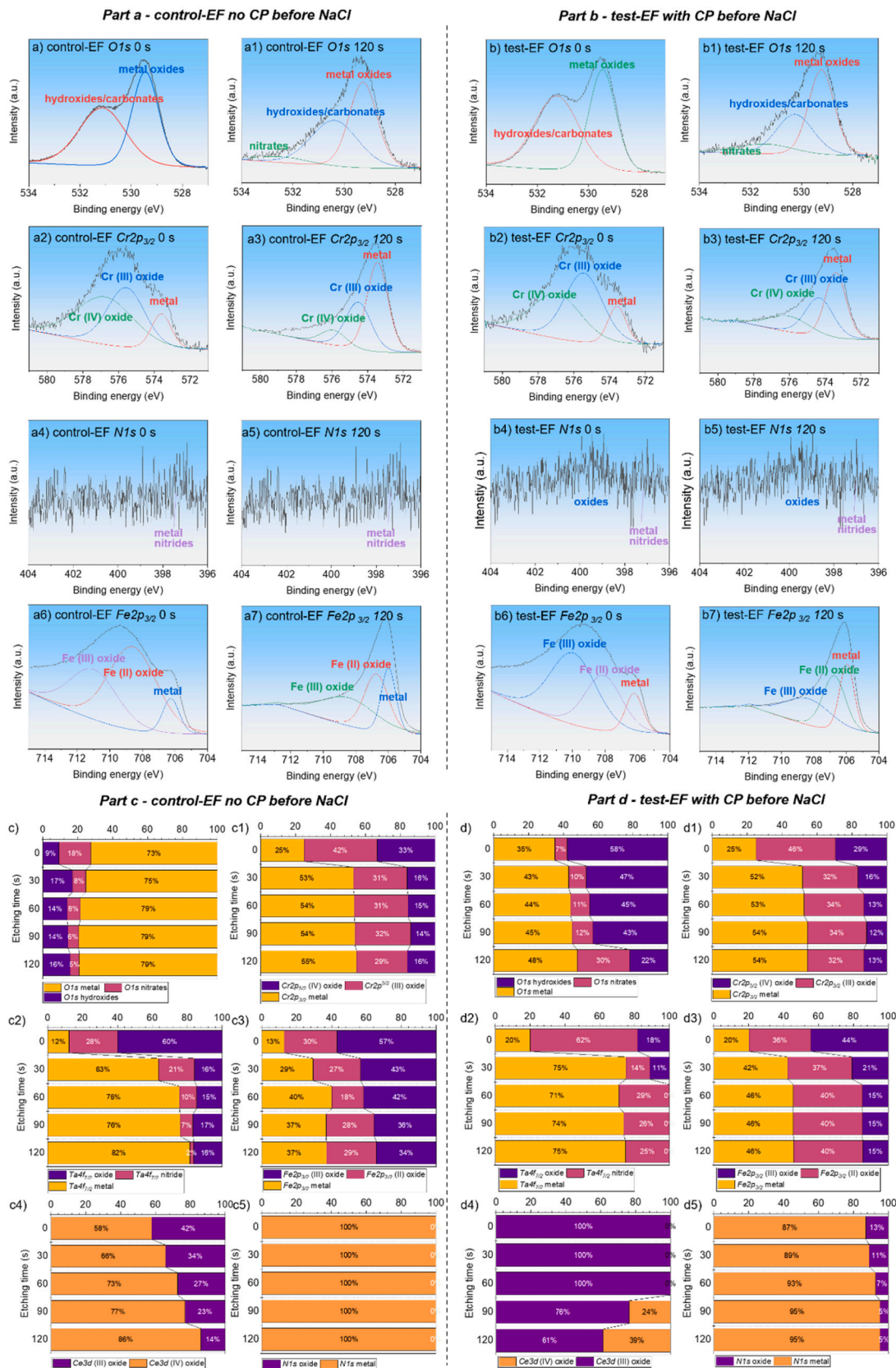
0.52 nm.

Fig. 4. Parts a and b show XPS spectra and peak fitting for both samples, control-EF (without CP) and test-EF (with CP), before exposure to NaCl at ambient conditions for selected alloying elements O, Cr, N and Fe. Parts c and d represent in-depth profile (0 s- 120 s etch time) of control-EF and test-EF samples for O, Cr, Ta, Fe, Ce and N.

oxides was observed from 0 s to 120 s of the in-depth profile. The main difference is in the composition most of the oxide for control-EF is from Fe (III) oxide and in test-EF the predominate specie is Fe (II) oxide (Fig. 4c3&d3). Observations for *Ce3d* peak is that in control-EF sample throughout all in-depth profile the presence of Ce (III) oxide is observed with decreasing intensity towards bulk, whereas in test-EF sample the Ce (IV) oxide is observed to be present only towards the bulk (after 90 s and 120 s) (Fig. 4c4&d4). The presence of Ce (III) throughout the oxide layer in the test-EF sample and in higher amounts compared to the control-EF sample can result in a more protective passive layer on the test-EF sample. For the *N1s* peak the results show that for both samples' N is present in an un-oxidised state (Fig. 4c5&d5). The difference is observed in the presence of also oxidised N in the test-EF sample, whereas it was not observed in the control-EF.

3.3. Structure of oxide film after corrosion in 30 wt% aqueous solution NaCl

Fig. 5a-b shows the results of curve-fitted spectra of *O1s, Cr2p$_{3/2}$, N1s* and *Fe2p$_{3/2}$* of in-depth etching spectra (0–120 s with 30 s interval) of conventionally (control-EF) and cryogenically processed (test-EF) samples (see Supplementary Material 2c-**d** for survey(s)). The passivation layer thickness (Supplementary Material 3c-**d**) for both samples, control-EF and test-EF, after exposure to 30 wt% NaCl for 24 h (based on *O1s* and *Fe2p* profiles selected as indicators), showed the thickness for the control EF sample roughly 0.52 nm and for the test-EF sample (with CP) to be approximately 0.54 nm. The XPS analysis showed which elements and oxidation states play an important role in the formed passive layer in each sample (control-EF or test-EF). In both samples for the *O1s* spectra (0 s −120 s etch time) (Figs. 5a-a1&b-b1) the following compounds are present: nitrates, chlorates, hydroxides and metal oxides. With higher depth, higher intensity and presence of metal oxides and chlorates. Furthermore, detailed study showed that test-EF sample has a higher presence of nitrates near the bulk compared to the control-EF, and a lower content of metal oxides compared to control-EF (Fig. 5c&d). For *Cr2p$_{3/2}$* for both samples (Fig. 5a2-a3&b2-b3). In the control and the test samples, Cr metal peaks, Cr (III) and Cr (IV) oxide states were present (Fig. 5c1&d1), whereas in test sample also presence of nitride/nitrates can be detected, almost until the end of etching. In the control sample, the oxide layer is mostly composed of Cr (III) oxide, while in the test sample the structure changes from mostly nitride to mostly Cr (III) oxide after 30 s etching and to mostly Cr (IV) oxide after 60 s etching. The results for N, *N1s*, showed the presence of oxidised N (nitrate), un-oxidised N and ammonium salt for both samples, control and test, at 0 s. After 120 s of etching, only the presence of the metal peak was observed for the test-EF sample (Fig. 5a4-a5&b4-b5). Closer observation showed that the oxidation state of nitrate and ammonium was gone after 60 s in the test-EF sample (Fig. 5c5&d5). Observation of Fe, *Fe2p$_{3/2}$*, showed three main oxidation state of metal, Fe (II) and Fe (III) oxide for both samples (Fig. 5a6-a7&b6-b7). In the control-EF sample at 0 s the oxide layer is mostly composed of Fe (III) oxide, afterward at 120 s toward bulk the state change to predominate composition metal peak (Fig. 5c3). For the test-EF sample Fig. 5d3 shows that the oxide layer at 0 s etching is mainly composed of Fe (II) and Fe (III) oxides. At 60 s of etching also two additional oxidation states of metal and complex oxides with possible nitrates occur, afterwards the peak of complex oxidation state is gone, this could indicate changes in the oxide layer which could lead to the changes in the passivation layer build-up and later corrosion resistance.

Furthermore, Ta, Ce, Na and Cl oxidation states were also analysed. *Ta4f* oxidation state revealed that in the control-EF (Fig. 5c2), Ta is mostly in its metallic state, which mean that it doesn't play an important role in building the passivation layer.
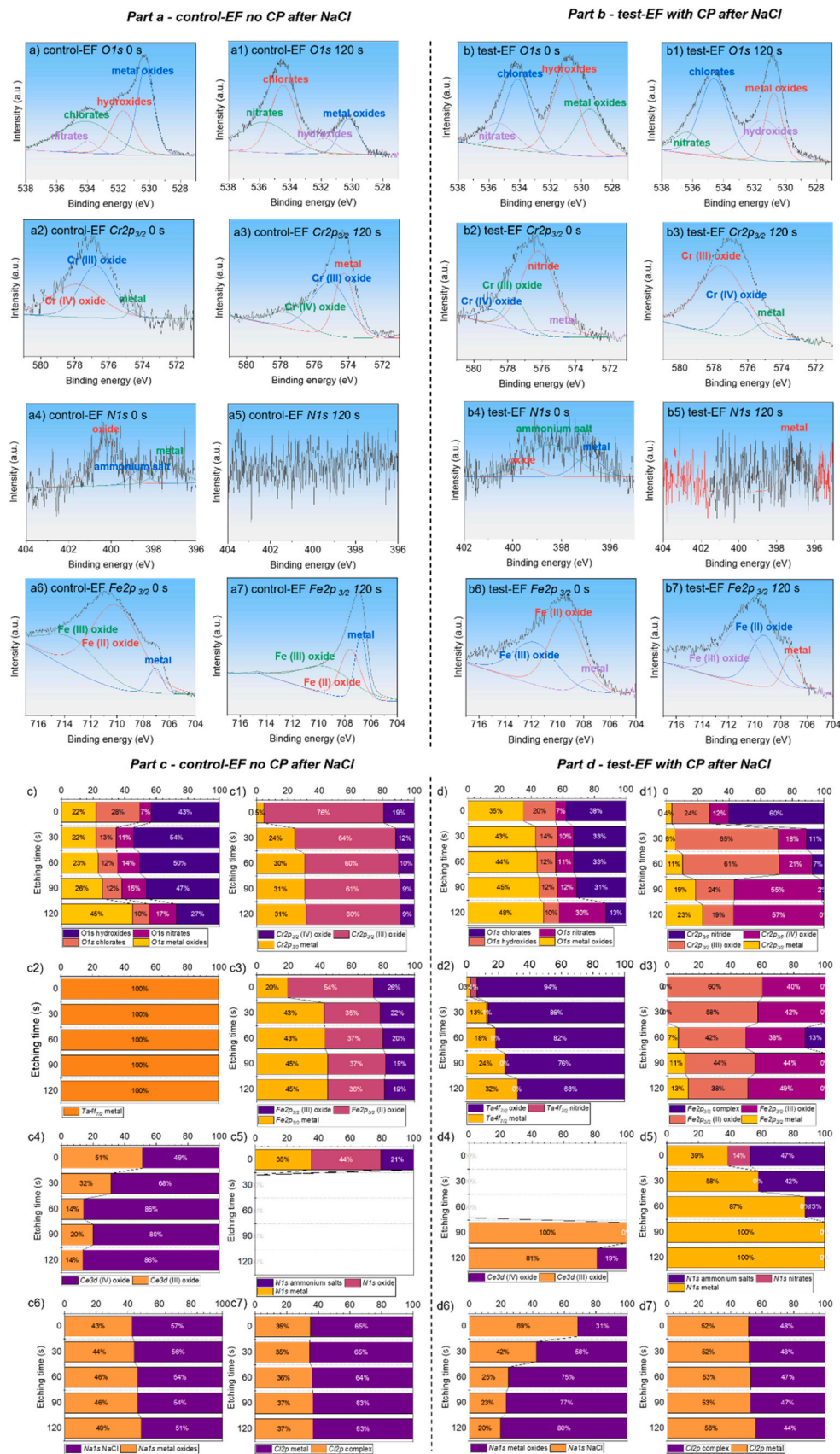
Compared with the test-EF (Fig. 5d2), where Ta clearly plays a role in the passivation player, where at surface (0 s) its presence as oxide, metal and nitride is detected, while after 120 s etch time only metal and

oxide oxidation state are present. For Ce (*Ce3d*) in control-EF sample at 0 s the oxide layer is mostly contains Ce in Ce (III) oxidation state, afterward at 120 s mostly from Ce (IV) oxidation state (Fig. 5c4). In the test sample (Fig. 5d4), the presence of Ce oxides in the Ce (III) oxidation state is detected only after 90 s of etching, and at 120 s etching time the structure is mostly of the same oxidation state and a smaller portion of the Ce (IV) oxidation state. This indicates that in conventionally heat-treated samples Ce is an important element in corrosion protection, whereas in cryogenically processed sample its role is not so predominant compared to other elements. Na and Cl elements were also monitored to detect any particular dynamics in the depth profile and passivation layer formation (Fig. 5c6-c7&d6-d7). For Na, *Na1s*, in the control sample an almost equal presence of metal oxide and Na in NaCl form was detected, whereas for chlorine, *Cl2p*, the similar ratio was observed from 0 s to 120 s etch time, with mostly metal oxidation state and some complex chlorine oxides. In the test-EF sample for *Na1s*, a lower presence of metal oxide state is observed until 60 s of etching and more NaCl, after which at 120 s etching time predominant presence of metal oxides is observed. For chlorine, *Cl2p*, a similar observation as for the control sample is also observed in the test sample.

These XPS-based observations indicate a complex formation of the passivation layer in test-EF, which is different compared to control-EF. Further FT-IR, AR-XPS and Raman shift spectroscopy (RS) tests were carried out to better understand the formation of oxides and corrosion behaviour of both samples.

AR-XPS (Fig. 6a&b) was performed to obtain better information of the outermost oxide layers for the most important elements in the passive layers, such as O, Cr, Fe and N. AR-XPS showed for *O1s*, for both samples with higher angle (90°) more metal peaks are present compared to lower angles (15–75°). The difference between the two samples is that in the test-EF sample a higher presence of chlorates, nitrates and hydroxides is observed compared to the control-EF sample. Observation of Cr (Fig. 6a1&b1), *Cr2p$_{3/2}$*, indicated a different composition of the test-EF sample compared to the control-EF sample. In test-EF sample with higher angle, not only higher percentage of metal peak but also Cr (IV) oxidation peak was observed compared to control-EF sample where higher concentration of Cr (III) oxidation peak was observed. These results are consistent with the deep etching observations. For Fe (Fig. 6a2&b2), *Fe2p$_{3/2}$*, the interesting observation showed the presence of complex Fe oxides and hydroxides for both samples with higher angle of observation, other observations are consisted with the depth profile. For the last observed element-N (Fig. 6a3&b3), *N1s*, the AR-XPS study displays a high presence of ammonium salts for both samples, which is correlated with the presence of N within the matrix and additionally, in the cryogenically processed sample (test-EF), with exposure to liquid N_2, as demonstrated by Jovičević-Klug et al. [18,19] and [17]. However, for a deeper understanding and observation of the formation of the passivation layer, a longer study with longer exposure times (6 months, 1 year, etc.) with different NaCl concentrations is needed to provide more answers as to how the cryogenic effect influences the unique and complex improvement of corrosion resistance.

FT-IR spectra were also obtained to identify possible Fe oxides and other oxides species (Fig. 7a). These results are consistent with other analytical techniques used in this work, such as XPS and RS. Fe bound to Cl oxides could be identified as a band around 1700 cm^{-1}. Ammonium salts were present on the surface of the samples at wave numbers around 958 and 920 cm^{-1}. The chlorates and ammonium compounds were also identified using the XPS technique. Goethite (α-FeOOH) was present at 806 and 648 cm^{-1}, akageneite (β-FeOOH) at 1420 and 660 cm^{-1}, lepidocrocite (γ-FeOOH) at 735 cm^{-1} and δ-FeOOH at 1118 cm^{-1}. These Fe oxide hydroxide compounds are reported in the literature in works using infrared spectroscopy[37,38]. Maghemite (γ-Fe$_2$O$_3$) was identified at 680 cm^{-1} [37,38]. Also, as results indicate around 800 cm^{-1} could also be present Fe$_2$(OH)$_3$Cl[37]. An interesting observation could be made around the wavenumbers between 800 and 700 cm^{-1}; there is a decrease in the absorption intensity present in the sample, which could
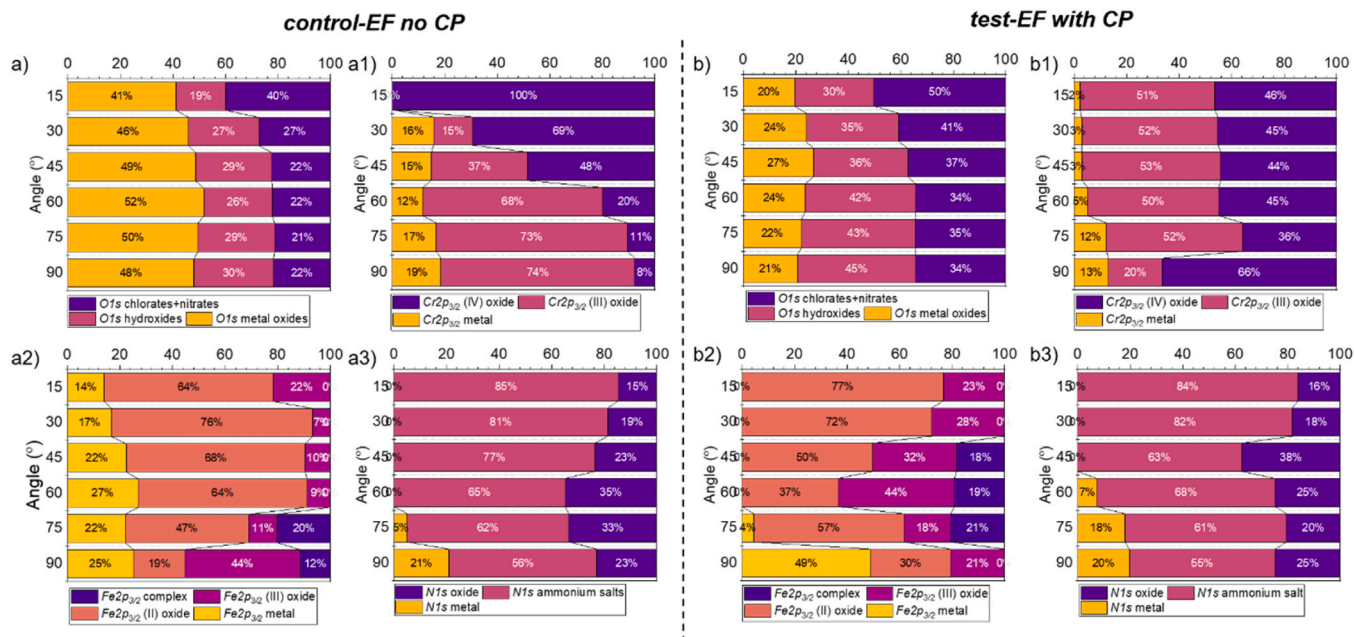
Fig. 5. Parts a and b show XPS spectra and peak fitting for both samples after immersion in 30 wt% NaCl solution at ambient conditions, control-EF (without CP) and test-EF (with CP), for selected alloying elements O, Cr, N and Fe. Parts c and d represent in-depth profile (0 s- 120 s) of control-EF and test-EF samples for O, Cr, Ta, Fe, Ce, N, Na and Cl.

Fig. 6. AR-XPS data for different angles for both samples (control-EF (no CP) and test-EF (with CP)) after immersion in 30 wt% NaCl aqueous solution for selected alloying elements O, Cr, N and Fe at ambient conditions.
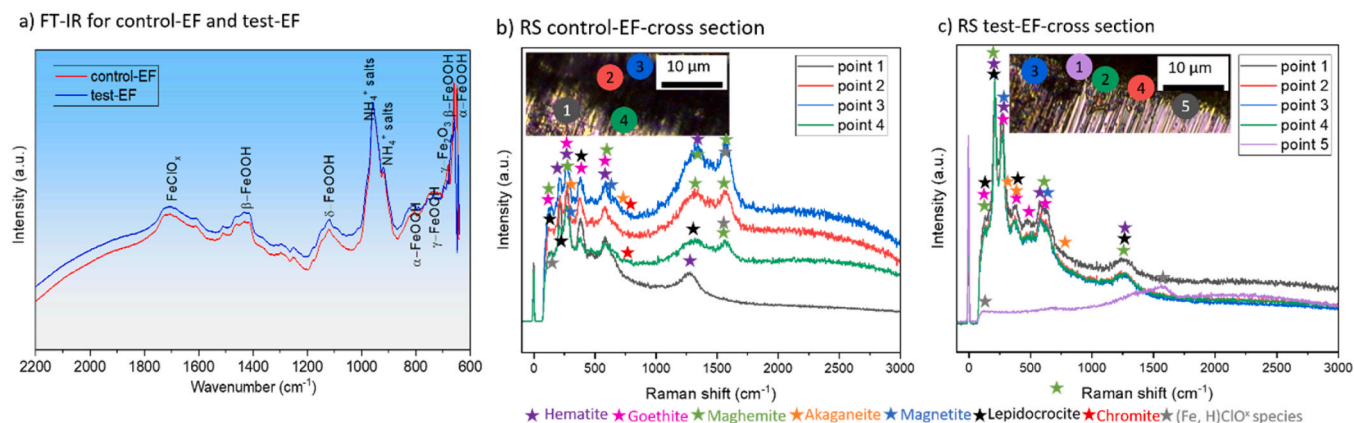

Fig. 7. a) Spectra obtained on control ant test EUROFER97 samples showing the presence of different Fe oxides with FT-IR. b-c) Raman shift spectroscopy (RS) for control sample, control-EF and test sample, test-EF after exposure in 30 wt% NaCl aqueous solution at ambient conditions.

probably be related to other species mixed with the Fe oxides-hydroxides. Raman shift spectroscopy (Fig. 7b&c) was used to provide information on the oxide species present in each heat-treated group. RS was performed on cross-section of both samples exposed to 30 % NaCl for 24 h to observe the formation of different oxide species in cross-section (points 1–4 for sample control-EF and points 1–5 for test-EF). Cross-section of both samples showed presence of hematite (Fe_2O_3), goethite (α-FeOOH), maghemite (γ-Fe_2O_3), akageneite (β-FeOOH), magnetite (Fe_3O_4), lepidocrocite (γ-FeOOH) and (Fe, H, N) ClO^x species[39–42]. In addition, chromite was also observed in the control-EF sample, but not in the test-EF sample. The (Fe, H, N)ClO^x species can also be correlated with the complex ammonium salts detected by XPS and FT-IR, mainly for the test-EF sample.

All these results indicate a clearly different development of the oxide/passivation layer of different heat-treated samples of EUROFER97 by different main components. For the control-EF (no CP) sample, the main elements that form the oxide layer are Cr, Fe, O, Ce and to some degree also N from the matrix. Similar observations were made in different test heat treatments and corrosion conditions observed by

Terada et al. [13] and Duerrschnabel et al. [16]. However, the observations made cryogenically processed EUROFER97 showed a different trend in the oxide/passive film formation, which showed important role of Cr, Fe, O, Ta and N, which is partially from matrix and partially enriched at the surface after CP. From this it can be confirmed that exposure in liquid N_2 for 24 h influences on the structure of the oxide/passivation layers that form on the surface if the two differently treated samples. For the cryogenically processed sample (test-EF) it was shown that a special layer enriched with N is formed, which could play an important role in corrosion resistance (see next section).

For the test-EF sample, it was also shown that a higher presence of ammonia, which could be mixed with oxides and hydroxides and form green rust, could act as an effective medium for improving corrosion resistance. Certainly, the ratio and thickness of the different oxides play an additional role in corrosion resistance.

3.4. Potentiodynamic polarisation measurements

Fig. 8 shows the results of potentiodynamic polarisation

measurements in 30 wt% NaCl carried out on the control-EF and test-EF. The corrosion potentials (*Ecorr*) of the control-EF and test-EF samples were −635 and −496 mV vs Ag/AgCl, respectively. The corrosion current densities (*icorr*) values obtained from the curves for the control-EF and test-EF samples are 2.65 and 0.034 μA/cm^2, respectively. The lower corrosion current density in the case of test-EF sample and the higher (more noble) corrosion potential could arise from the inherent differences in the protective oxide layer formed on the surface. The N introduced in the matrix by the cryogenic processing is likely to result in an increased corrosion resistance [17,18,43–46]. Furthermore, the lower content of Cr in the matrix after CP, shifts the role to Fe and N, as shown with XPS, which causes different current density, which plays and additional factor in shifting the curve for test-EF. The other important difference in the passive layers formed on the control-EF and the test-EF samples is the presence of Ce(III) on the surface oxide, as well as in higher amounts than Ce(IV) in the test-EF sample (Fig. 4. d4). Ce(III) is a well-known corrosion inhibitor due to its ability to form a stable passive layer[47–49].

The improved corrosion behaviour observed in the test-EF sample is therefore proposed to be a result of the synergetic effect of inclusion of N during the cryogenic processing and enrichment of Ce(III) species. This results in shifting of the *Ecorr* to more passive potentials and *icorr* to lower values, although the oxide layer on the surface is depleted of protective chromium oxide species.

4. Conclusions

The conclusions of this study are important and relevant not only to the energy sector but also to the materials and cryogenic society. The influence of cryogenic processing (CP) on the microstructure, oxide formation and corrosion resistance of EUROFER97 can be summarised as follows: (1) Both control and test-EF samples consist mainly of a martensitic matrix. The presence of MC, M_6C, M_3C_2, M_7C_3 and $M_{23}C_6$ carbides were observed in both groups. In the test-EF group (with CP) it can be also observed that the matrix is enriched with Fe compared to the control-EF, which indicates the increased precipitation of carbides and also that Fe is the main element that builds up oxides. (2) APT results confirm that the Ce-oxides are located close to or above the carbides and have an inner and outer shell composed of different REEs. (3) The study shows a different development of the passive layer before and after the immersion in NaCl aqueous solution at ambient conditions in the control and test samples. In the CP-treated sample, the important role of oxide formation is shifted to Fe and N, compared to the control sample where Cr and Ce oxides also play an important role. (4) Potentiodynamic polarization measurements show improved corrosion behaviour of cryogenically treated sample, which is suggested to be correlated to the synergetic effect of N introduced into the matrix by the cryogenic processing and enrichment of Ce(III) on the surface oxide, resulting in increased corrosion resistance.

Funding

CRediT authorship contribution statement

Patricia Jovičević-Klug: Writing – review & editing, Writing – original draft, Visualization, Validation, Methodology, Investigation, Formal analysis, Conceptualization. **J. Manoj Prabhakar:** Writing – review & editing, Writing – original draft, Visualization, Methodology, Investigation, Formal analysis. **Cristiano Kasdorf Giesbrecht:** Writing
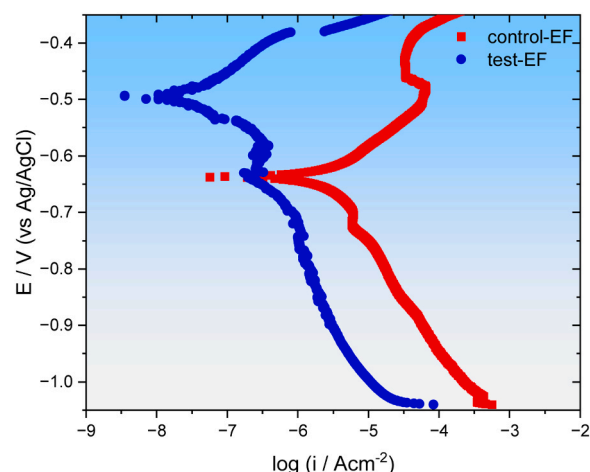

Fig. 8. Potentiodynamic polarization measurements on control-EF and test-EF samples in 30 wt% NaCl aqueous solution at ambient conditions.

– review & editing, Writing – original draft, Visualization, Methodology, Investigation, Formal analysis. **Michael Rohwerder:** Writing – review & editing, Supervision, Resources. **Tim M. Schwarz:** Writing – review & editing, Methodology, Formal analysis. **Michael Rieth:** Writing – review & editing, Supervision, Resources. **Carsten Bonnekoh:** Writing – review & editing, Resources.

Declaration of Competing Interest

The authors declare that they have no known competing financial interests or personal relationships that could have appeared to influence the work reported in this paper.

Appendix A. Supporting information

Supplementary data associated with this article can be found in the online version at doi:10.1016/j.corsci.2025.112691.

Data availability

Data will be made available on request.

References

[1] T. Sparks, V. Kuksenko, M. Gorley, J. Hoffmann, Y.L. Chiu, T. Connolley, M. Rieth, Y. Wang, B. Cai, In-Situ synchrotron investigation of elastic and tensile properties of oxide dispersion strengthened EUROFER97 steel for advanced fusion reactors, Acta Mater. 271 (2024) 119876, https://doi.org/10.1016/J. ACTAMAT.2024.119876.

[2] R. Lindau, A. Möslang, M. Rieth, M. Klimiankou, E. Materna-Morris, A. Alamo, A.A. F. Tavassoli, C. Cayron, A.M. Lancha, P. Fernandez, N. Baluc, R. Schäublin, E. Diegele, G. Filacchioni, J.W. Rensman, B.V.D. Schaaf, E. Lucon, W. Dietz, Present development status of EUROFER and ODS-EUROFER for application in blanket concepts, Fusion Eng. Des. 75–79 (2005) 989–996, https://doi.org/10.1016/J. FUSENGDES.2005.06.186.

[3] P. Jovičević-Klug, M. Rohwerder, Sustainable new technology for the improvement of metallic materials for future energy applications, Coatings 13 (2023) 1822, https://doi.org/10.3390/COATINGS13111822.

[4] P. Jovičević-Klug, C. Bonnekoh, M. Jovičević-Klug, B. Ambrožič, G. Dražić, Z. Miłosz, Y. Ma, I. McCarroll, B. Breitbach, M. Amati, L. Gregoratti, M. Rieth, M. Rohwerder, Designing advanced high-Cr ferrous alloys for next-generation energy applications through cryogenic processing, Appl. Surf. Sci. 665 (2024) 160290, https://doi.org/10.1016/j.apsusc.2024.160290.

[5] M. Duerrschnabel, U. Jäntsch, R. Gaisin, M. Rieth, Microstructural insights into EUROFER97 batch 3 steels, Nucl. Mater. Energy 35 (2023) 101445, https://doi. org/10.1016/J.NME.2023.101445.

[6] M. Klimenkov, U. Jäntsch, M. Rieth, A. Möslang, Correlation of microstructural and mechanical properties of neutron irradiated EUROFER97 steel, J. Nucl. Mater. 538 (2020) 152231, https://doi.org/10.1016/J.JNUCMAT.2020.152231.

[7] S. Ningshen, M. Sakairi, K. Suzuki, S. Ukai, The passive film characterization and anodic polarization behavior of 11% Cr ferritic/martensitic and 15% Cr oxide

dispersion strengthened steels in different electrolytic solutions, Appl. Surf. Sci. 274 (2013) 345–355, https://doi.org/10.1016/J.APSUSC.2013.03.059.

[8] K. Mukai, F. Sanchez, R. Knitter, Chemical compatibility study between ceramic breeder and EUROFER97 steel for HCPB-DEMO blanket, J. Nucl. Mater. 488 (2017) 196–203, https://doi.org/10.1016/J.JNUCMAT.2017.03.018.

[9] M. Duerrschnabel, E. Gaisina, R. Gaisin, M. Walter, J. Aktaa, M. Rieth, Nanoscale insights into the corrosion of EUROFER by lithium ceramics, Corros. Sci. 199 (2022) 110190, https://doi.org/10.1016/J.CORSCI.2022.110190.

[10] T. Hernández, P. Fernández, Effect of the environment on the corrosion of EUROFER97 by solid lithium breeders, J. Nucl. Mater. 447 (2014) 160–165, https://doi.org/10.1016/J.JNUCMAT.2013.12.026.

[11] P. Fernández, A.M. Lancha, J. Lapeña, M. Serrano, M. Hernández-Mayoral, Metallurgical properties of reduced activation martensitic steel Eurofer'97 in the as-received condition and after thermal aging, J. Nucl. Mater. 307–311 (2002) 495–499, https://doi.org/10.1016/S0022-3115(02)01013-9.

[12] L. Verma, V.V. Dabhade, Investigation of nano-clusters evolved with Ti and Zr in ferritic ODS steel and their effect on microstructure and mechanical properties, Mater. Today Commun. 40 (2024) 109943, https://doi.org/10.1016/J.MTCOMM.2024.109943.

[13] M. Terada, A.J. De Oliveira Zimmermann, H.R.Z. Sandim, I. Costa, A.F. Padilha, Corrosion behavior of Eurofer 97 and ODS-Eurofer alloys compared to traditional stainless steels, J. Appl. Electrochem 41 (2011) 951–959, https://doi.org/10.1007/S10800-011-0320-1/FIGURES/10.

[14] R. Boullon, J.C. Jaboulay, J. Aubert, Molten salt breeding blanket: Investigations and proposals of pre-conceptual design options for testing in DEMO, Fusion Eng. Des. 171 (2021) 112707, https://doi.org/10.1016/J.FUSENGDES.2021.112707.

[15] K.G. Gareev, Diversity of iron oxides: mechanisms of formation, physical properties and applications, Magnetochemistry 9 (2023) 119, https://doi.org/10.3390/MAGNETOCHEMISTRY9050119.

[16] M. Duerrschnabel, E. Gaisina, R. Gaisin, M. Walter, J. Aktaa, M. Rieth, Nanoscale insights into the corrosion of EUROFER by lithium ceramics, Corros. Sci. 199 (2022) 110190, https://doi.org/10.1016/J.CORSCI.2022.110190.

[17] P. Jovičević-Klug, M. Jovičević-Klug, B. Podgornik, Unravelling the role of nitrogen in surface chemistry and oxidation evolution of deep cryogenic treated high-alloyed ferrous alloy, Coatings 12 (2022) 213, https://doi.org/10.3390/COATINGS12020213.

[18] P. Jovičević-Klug, T. Kranjec, M. Jovičević-Klug, T. Kosec, B. Podgornik, Influence of the deep cryogenic treatment on AISI 52100 and AISI D3 Steel's corrosion resistance, Materials 14 (2021) 6357, https://doi.org/10.3390/MA14216357.

[19] M. Jovičević-Klug, P. Jovičević-Klug, T. Kranjec, B. Podgornik, Cross-effect of surface finishing and deep cryogenic treatment on corrosion resistance of AISI M35 steel, J. Mater. Res. Technol. 14 (2021) 2365–2381, https://doi.org/10.1016/j.jmrt.2021.07.134.

[20] E. Materna-Morris, C. Adelhelm, S. Baumgärtner, B. Dafferner, P. Graf, S. Heger, U. Jäntsch, R. Lindau, C. Petersen, M. Rieth, R. Ziegler, H. Zimmermann, F. Karlsruhe, 2007, Final Report on the EFDA Task STRUCTURAL MATERIAL EUROFER97-2, Characterization of Rod and Plate Material: Structural, Tensile, Charpy, and Creep Properties.

[21] K. Thompson, D. Lawrence, D.J. Larson, J.D. Olson, T.F. Kelly, B. Gorman, In situ site-specific specimen preparation for atom probe tomography, Ultramicroscopy 107 (2007) 131–139, https://doi.org/10.1016/j.ultramic.2006.06.008.

[22] G.H. Major, N. Fairley, P.M.A. Sherwood, M.R. Linford, J. Terry, V. Fernandez, K. Artyushkova, Practical guide for curve fitting in x-ray photoelectron spectroscopy, J. Vac. Sci. Technol. A 38 (2020), https://doi.org/10.1116/6.0000377.

[23] S. Tougaard, Practical guide to the use of backgrounds in quantitative XPS, J. Vac. Sci. Technol. A 39 (2021), https://doi.org/10.1116/6.0000661.

[24] J.W. Pinder, G.H. Major, D.R. Baer, J. Terry, J.E. Whitten, J. Čechal, J.D. Crossman, A.J. Lizarbe, S. Jafari, C.D. Easton, J. Baltrusaitis, M.A. van Spronsen, M.R. Linford, Avoiding common errors in X-ray photoelectron spectroscopy data collection and analysis, and properly reporting instrument parameters, Appl. Surf. Sci. Adv. 19 (2024) 100534, https://doi.org/10.1016/J.APSADV.2023.100534.

[25] P. Jovičević-Klug, J.M. Prabhakar, C.K. Giesbrecht, T.M. Schwarz, C. Bonnekoh, M. Rieth, M. Rohwerder, Hydrogen diffusion and trapping in a cryogenic processed high-Cr ferrous alloy, Npj Mater. Degrad. 2024 8:1 8 (2024) 1–9, https://doi.org/10.1038/s41529-024-00522-1.

[26] Z. Adabavazeh, W.S. Hwang, Y.H. Su, Effect of Adding Cerium on Microstructure and Morphology of Ce-Based Inclusions Formed in Low-Carbon Steel, Sci. Rep. 2017 7:1 7 (2017) 1–10, https://doi.org/10.1038/srep46503.

[27] Y. Ji, M.X. Zhang, H. Ren, Roles of Lanthanum and Cerium in Grain Refinement of Steels during Solidification, Met. 2018, Vol. 8, Page 884 8 (2018) 884, https://doi.org/10.3390/MET8110884.

[28] E. Stoyanova, D. Nikolova, D. Stoychev, P. Stefanov, T. Marinova, Effect of Al and Ce oxide layers electrodeposited on OC4004 stainless steel on its corrosion characteristics in acid media, Corros. Sci. 48 (2006) 4037–4052, https://doi.org/10.1016/J.CORSCI.2006.04.008.

[29] R. Silva, D.J. Young, C.B.M. Junior, G.S. Vacchi, C.A.T. Alberto, A.M. de, S. Malafaia, C. Pascal, C.A.D. Rovere, Role of cerium addition in enhancing the oxidation resistance of austenitic Fe-Mn-Si-Cr-Ni shape memory stainless steels at 800 °C: Microstructure and oxidation mechanism, Corros. Sci. 209 (2022) 110788, https://doi.org/10.1016/J.CORSCI.2022.110788.

[30] E. Stoyanova, D. Stoychev, Corrosion Behaviour of Stainless Steels Modified by Cerium Oxide Layers, in: H. Shih (Ed.), Corrosion Resistance, InTech, Rijeka, Croatia, 2012, p. 239.

[31] L. Hao, Z. Jiang, Y. Fang, Y. Zhou, B. Fu, L. Lin, Understanding the role of oxygen vacancy on corrosion resistance of coating containing cerium oxide nanoparticles doped with cobalt as highly effective corrosion inhibitors, Appl. Surf. Sci. 626 (2023) 157300, https://doi.org/10.1016/J.APSUSC.2023.157300.

[32] Y.C. Lu, M.B. Ives, The improvement of the localized corrosion resistance of stainless steel by cerium, Corros. Sci. 34 (1993) 1773–1785, https://doi.org/10.1016/0010-938X(93)90015-9.

[33] G.J. Cai, C.S. Li, Effects of Ce on inclusions and corrosion resistance of low-nickel austenite stainless steel, Mater. Corros. 66 (2015) 1445–1455, https://doi.org/10.1002/MACO.201508380.

[34] B. Gault, D.W. Saxey, M.W. Ashton, S.B. Sinnott, A.N. Chiaramonti, M.P. Moody, D. K. Schreiber, Behavior of molecules and molecular ions near a field emitter*, N. J. Phys. 18 (2016) 033031, https://doi.org/10.1088/1367-2630/18/3/033031.

[35] D.W. Saxey, Correlated ion analysis and the interpretation of atom probe mass spectra, Ultramicroscopy 111 (2011) 473–479, https://doi.org/10.1016/J.ULTRAMIC.2010.11.021.

[36] J. Hufenbach, A. Helth, M.H. Lee, H. Wendrock, L. Giebeler, C.Y. Choe, K.H. Kim, U. Kühn, T.S. Kim, J. Eckert, Effect of cerium addition on microstructure and mechanical properties of high-strength Fe85Cr4Mo8V2C1 cast steel, Mater. Sci. Eng.: A 674 (2016) 366–374, https://doi.org/10.1016/J.MSEA.2016.07.114.

[37] R. Jasinski, A. Iob, FTIR Measurements of Iron Oxides on Low Alloy Steel, J. Electrochem Soc. 135 (1988) 551–556, https://doi.org/10.1149/1.2095656/XML.

[38] A. Raman, B. Kuban, A. Razvan, The application of infrared spectroscopy to the study of atmospheric rust systems—I. Standard spectra and illustrative applications to identify rust phases in natural atmospheric corrosion products, Corros. Sci. 32 (1991) 1295–1306, https://doi.org/10.1016/0010-938X(91)90049-U.

[39] H.B. Wang, Y. Li, G.X. Cheng, W. Wu, Y.H. Zhang, X.Y. Li, Electrochemical Investigation of Corrosion of Mild Steel in NH4Cl Solution, Int J. Electrochem Sci. 13 (2018) 5268–5283, https://doi.org/10.20964/2018.06.05.

[40] H.H. Eysel, Raman intensities of liquids: absolute scattering activities and Cl–O bond EOPs of ClO−, ClO−2, ClO−3 and ClO−4 ions in aqueous solution, Spectrochim. Acta A 44 (1988) 991–997, https://doi.org/10.1016/0584-8539(88)80218-6.

[41] H. Zhou, Z. Chen, Z. Bai, Study on the effects of the surface temperature on the formation of ammonium chloride and fly ash deposits, Environ. Prog. Sustain Energy 39 (2020) e13367, https://doi.org/10.1002/EP.13367.

[42] M. Jovičević-Klug, Y. Ma, P. Jovičević-Klug, J.M. Prabhakar, M. Rohwerder, D. Raabe, Thermal Kinetics and Nitriding Effect of Ammonia-Based Direct Reduction of Iron Oxides, ACS Sustain Chem. Eng. 12 (2024) 9882–9896, https://doi.org/10.1021/ACSSUSCHEMENG.4C02363/ASSET/IMAGES/LARGE/SC4C02363_0010.JPEG.

[43] P. Jovičević-Klug, L. Tegg, M. Jovičević-Klug, R. Parmar, M. Amati, L. Gregoratti, L. Almasy, J.M. Cairney, B. Podgornik, Understanding Carbide Evolution and Surface Chemistry during Deep Cryogenic Treatment in High-alloyed Ferrous Alloy, Appl. Surf. Sci. 610 (2023) 155497, https://doi.org/10.1016/j.apsusc.2022.155497.

[44] P. Jovičević-Klug, M. Jovičević-Klug, L. Tegg, D. Seidler, L. Thormahlen, R. Parmar, M. Amati, L. Gregoratti, J.M. Cairney, J. McCord, M. Rohwerder, B. Podgornik, Correlative surface and bulk analysis of deep cryogenic treatment influence on high-alloyed ferrous alloy, J. Mater. Res. Technol. 11–12 (2022) 4799–4810, https://doi.org/10.1016/j.jmrt.2022.11.075.

[45] U. Kamachi Mudali, P. Shankar, S. Ningshen, R.K. Dayal, H.S. Khatak, B. Raj, On the pitting corrosion resistance of nitrogen alloyed cold worked austenitic stainless steels, Corros. Sci. 44 (2002) 2183–2198, https://doi.org/10.1016/S0010-938X(02)00035-5.

[46] Y. Fu, X. Wu, E.H. Han, W. Ke, K. Yang, Z. Jiang, Effects of nitrogen on the passivation of nickel-free high nitrogen and manganese stainless steels in acidic chloride solutions, Electro Acta 54 (2009) 4005–4014, https://doi.org/10.1016/J.ELECTACTA.2009.02.024.

[47] S. Kallip, A.C. Bastos, K.A. Yasakau, M.L. Zheludkevich, M.G.S. Ferreira, Synergistic corrosion inhibition on galvanically coupled metallic materials, Electrochem Commun. 20 (2012) 101–104, https://doi.org/10.1016/J.ELECOM.2012.04.007.

[48] K. Aramaki, The inhibition effects of cation inhibitors on corrosion of zinc in aerated 0.5 M NaCl, Corros. Sci. 43 (2001) 1573–1588, https://doi.org/10.1016/S0010-938X(00)00144-X.

[49] Y. Yin, M. Schulz, M. Rohwerder, Optimizing smart self-healing coatings: Investigating the transport of active agents from the coating towards the defect, Corros. Sci. 190 (2021) 109661, https://doi.org/10.1016/J.CORSCI.2021.109661.